J. Fluid Mech. (2001), *vol.* 435, *pp.* 55–80. Printed in the United Kingdom

Flow structures and particle deposition patterns in double-bifurcation airway models. Part 2. Aerosol transport and deposition

By J. K. COMER[1], C. KLEINSTREUER† AND C. S. KIM[2]

[1]Department of Mechanical and Aerospace Engineering, North Carolina State University, Raleigh, NC 27695-7910, USA

[2]Human Studies Division, National Health and Environmental Effects Research Laboratory, US EPA, Research Triangle Park, NC 27711, USA

(Received 10 May 1999 and in revised form 9 November 2000)

The flow theory and air flow structures in symmetric double-bifurcation airway models assuming steady laminar, incompressible flow, unaffected by the presence of aerosols, has been described in a companion paper (Part 1). The validated computer simulation results showed highly vortical flow fields, especially around the second bifurcations, indicating potentially complex particle distributions and deposition patterns. In this paper (Part 2), assuming spherical non-interacting aerosols that stick to the wall when touching the surface, the history of depositing particles is described. Specifically, the finite-volume code CFX (AEA Technology) with user-enhanced FORTRAN programs were validated with experimental data of particle deposition efficiencies as a function of the Stokes number for planar single and double bifurcations. The resulting deposition patterns, particle distributions, trajectories and time evolution were analysed in the light of the air flow structures for relatively low ($Re_{D_1} = 500$) and high ($Re_{D_1} = 2000$) Reynolds numbers and representative Stokes numbers, i.e. $St_{D_1} = 0.04$ and $St_{D_1} = 0.12$. Particle deposition patterns and surface concentrations are largely a function of the local Stokes number, but they also depend on the fluid–particle inlet conditions as well as airway geometry factors. While particles introduced at low inlet Reynolds numbers (e.g. $Re_{D_1} = 500$) follow the axial air flow, secondary and vortical flows become important at higher Reynolds numbers, causing the formation of particle-free zones near the tube centres and subsequently elevated particle concentrations near the walls. Sharp or mildly rounded carinal ridges have little effect on the deposition efficiencies but may influence local deposition patterns. In contrast, more drastic geometric changes to the basic double-bifurcation model, e.g. the 90°-non-planar configuration, alter both the aerosol wall distributions and surface concentrations considerably.

1. Introduction

In this article's companion paper, Part 1 (Comer, Kleinstreuer & Zhang 2001), the theoretical basis and computer simulation results of air flow fields for three generations of the respiratory tract represented by glass airway models (see Weibel 1963) were described. The assumption of one-way coupling between carrier fluid

† Author to whom correspondence should be addressed: e-mail ck@eos.ncsu.edu

and dispersed aerosol allowed the air flow analysis to be carried out independently. In this paper (Part 2), the transport and deposition of aerosols are discussed. The numerical results presented include the fate of each particle in relation to its starting position, representative particle trajectories, the Lagrangian time evolution of a volumetric particle pulse, particle dispersion driven by the local vortical air flow, and particle deposition patterns. Specifically, in § 2, the particle trajectory equation and numerical solution method are outlined. Comparisons with measured particle deposition efficiencies, $\eta = \eta(St)$, are given in § 3, which also contains all the simulation results listed previously. The work is summarized in § 4.

While most researchers have focused on particle deposition in single bifurcation models (see Kinsara, Tompson & Loyalka 1993; Balásházy & Hofmann 1993, 1995; Balásházy 1994; Gatlin *et al.* 1997), Lee, Goo & Chung (1996) computed the velocity field, particle trajectories, and deposition efficiencies for two- and three-dimensional single and double bifurcations at one Reynolds number, $Re = 500$. They postulated that the true, *in vivo*, deposition efficiency could be modelled accurately using the deposition results from the second generation of a double-bifurcation model. Their results indicate that the deposition efficiency (DE) in the second bifurcation is always less than in the first bifurcation, and the DE in the second bifurcation of a planar configuration is larger than that of a non-planar configuration. Unfortunately, neither correlations for the deposition efficiency nor local particle deposition plots were given, thus it is not possible to utilize these results to gain further insight into the relationship between particle deposition and possible health effects. Furthermore, the discussion of the velocity field and its relationship to the particle distribution was limited, with only the planar symmetry velocity field given. The geometry used featured constant-diameter tubes (i.e. $D_1 = D_2 = D_3$), and 45° bifurcation angles which are not in physiological agreement with the human airways. The constant-diameter tubes reduce the flow resistance and the secondary flow at the bifurcations and, therefore, affect the particle deposition. Also of concern was the length of the daughter tubes used in their numerical simulations and possible numerical influences which are mistakenly attributed to the existence of a second bifurcation. For the single bifurcation study it appears that the mesh was terminated three diameters past the carina, that is, before the flow has become fully developed, at least at higher Reynolds numbers, i.e. $Re_D \geqslant 500$. This explains why the authors observed that attaching a second bifurcation resulted in fluid and particle flow fields which were different from the single bifurcation models.

Measurements of particle deposition in single bifurcating tube models have been provided by Johnston, Isles & Muri (1977), Kim & Iglesias (1989), and Kim *et al.* (1994). Recently, Kim & Fisher (1999) employed a double-bifurcation glass tube airway model following Weibel (1963), which is also the geometric system of the present analysis. Kim and his co-workers plotted particle deposition efficiencies, η, as a function of Stokes number, in the range $0.01 < St < 0.3$, for different geometries and inlet Reynolds numbers. Based on their mass balances, they emphasized the single-variable dependence of $\eta(St)$ and considered variations in flow rate, wall curvature, and local configurations as minor effects. It will turn out that variations in secondary parameters within bounds do not greatly affect the global mass balance, but they measurably influence the local particle deposition patterns and wall concentrations, which are key in health impact assessments (Comer *et al.* 2000).

2. Theory

The flow domain and gas transport equations were described in Part 1. The motion of particles suspended in this gas is governed by Newton's Second Law:

$$m_p \frac{\mathrm{d}\boldsymbol{v}_p}{\mathrm{d}t} = \sum \boldsymbol{F}_p \tag{2.1}$$

where m_p is the mass of a single, spherical particle, d_p is particle diameter in the range $3 \leqslant d_p \leqslant 7$ μm, and $\sum \boldsymbol{F}_p$ are the forces acting on it. In the light of the small particle Reynolds numbers, $Re_p \sim |\boldsymbol{v} - \boldsymbol{v}_p| \ll 1$ where $|\boldsymbol{v} - \boldsymbol{v}_p|$ is the slip velocity, a large particle-to-fluid density ratio, $\rho_p/\rho \gg 1$, and $d_p > 1\,\mu$m, most of the known particle forces other than the drag force can be discounted using order-of-magnitude arguments. First, these particles are relatively large, so Brownian motion and rarefied gas effects can be neglected. Second, the particulate material considered in this paper is far denser than air, causing terms that depend on this ratio, such as pressure force and buoyancy force, to be small. Of the lift forces, Magnus lift can be ignored because the particles are not spinning rapidly. It is harder to justify the neglect of the shear-induced (Saffman) lift force. We do so on grounds of pragmatism; no clear expression exists for the force in three-dimensional flows and the shear fields are much weaker for laminar flows than turbulent flows. Moreover, the resulting, simplified particle equation of motion, which produced excellent particle deposition results when compared with measurements (Kim & Fisher 1999), will make it easy to elucidate the physical processes at work. Hence, the final equation may be stated as

$$\frac{\mathrm{d}\boldsymbol{v}_p}{\mathrm{d}t} = \frac{18\mu}{d_p^2 \rho_p}(\boldsymbol{v} - \boldsymbol{v}_p)\phi_D \tag{2.2}$$

where ϕ_D is a correction to Stokes' drag force for finite particle Reynolds number based on the slip velocity $(\boldsymbol{v} - \boldsymbol{v}_p)$:

$$\phi_D = C_D \frac{Re_p}{24}, \tag{2.3}$$

C_D being Clift, Grace & Weber's (1978) empirical correction:

$$C_D = \begin{cases} 24/Re_p & \text{for} \quad 0 < Re_p \leqslant 1.0 \\ 24/Re_p^{0.646} & \text{for} \quad 1.0 < Re_p \leqslant 400, \end{cases} \tag{2.4}$$

and

$$Re_p = \rho |\boldsymbol{v} - \boldsymbol{v}_p| d_p/\mu. \tag{2.5}$$

The representative Stokes number range and associated parameter values are given in table 1. The justification for related inspiratory Reynolds numbers was outlined in table 2 of Part 1.

For the steady inhalation phase, a parabolic fluid velocity profile with an associated monodispersed spherical particle distribution (see figure 1*a*) were specified at the inlet. In the current study, a uniform pressure boundary condition is used for the outlets, which results in symmetric flow about the first carina, i.e. $y = 0$ (see figure 1*b*). In studies which are currently in progress this condition has been modified to measure the effects of the various levels of flow asymmetry. The initial particle velocities were set equal to that of the fluid and one-way coupling was assumed between the air and particle flow fields. The boundary conditions for the governing equations include symmetry with respect to the plane of the first bifurcation (i.e. $z = 0$), no fluid

Reynolds number	$Re_D = 500$	$Re_D = 2000$
Stokes number range		
$St_k = \frac{\rho_p d_p^2 Re_D}{\rho D^2 18}$	0.02–0.12	0.02–0.23
Particle diameter, d_p (μm)	3–7	3–7
Particle density, ρ_p (kg m^{-3})	2859–3150	715–1510

TABLE 1. Representative system parameters.

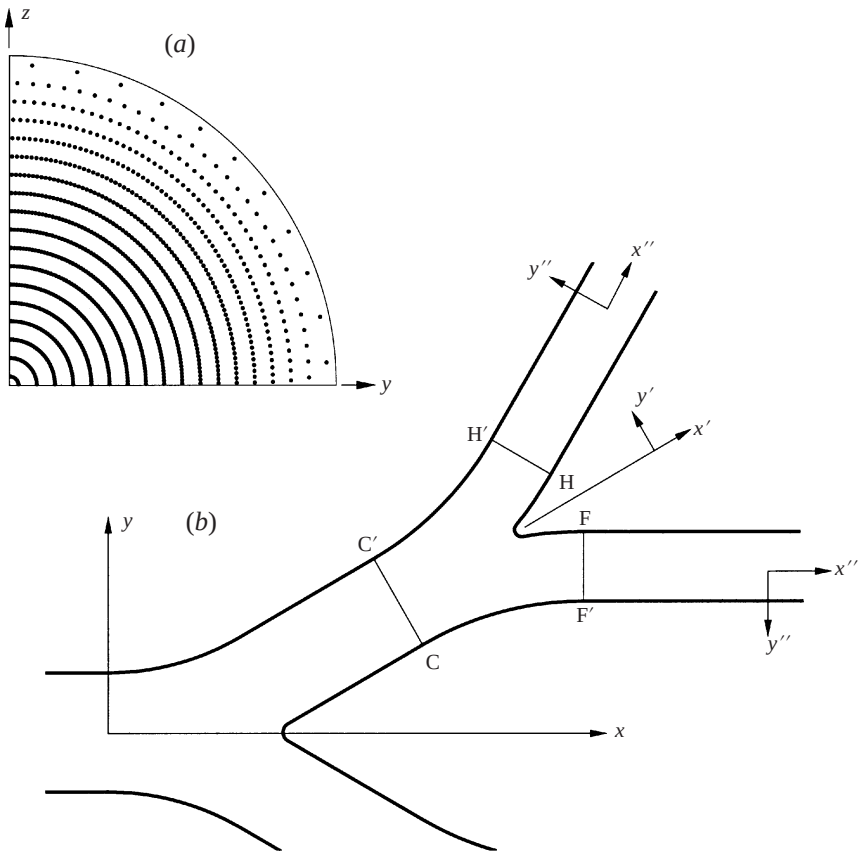

FIGURE 1. System diagram: (*a*) Schematic of quarter-plane inlet particle distribution; and (*b*) planar scale model of planar double bifurcation with coordinate systems and locations of particle cross-sections.

slip at the rigid impermeable walls, and particle deposition and withdrawal when the particle's centre comes within one radius from the wall, which mimics the experiments with oil-based spherical droplets (Kim *et al.* 1994; Kim & Fisher 1999) as well as the real-world scenario (Fox 1993).

The numerical solution of the fluid flow equations was carried out employing a user-enhanced commercial finite-volume-based program CFX 4.2 (AEA Technology

1997). The numerical program uses a structured, multi-block, body-fitted coordinate discretization scheme. The CFX equation solver is based on the SIMPLEC algorithm (Patankar 1983) with under-relaxation. The relaxation factor for the velocity is 0.65. All variables, including velocity components and pressure, are located at the centroids of the control volumes. An improved Rhie–Chow interpolation method was employed to obtain the velocity components and pressure on the control volume faces from those at the control volume centers. Hybrid differencing was used to model the convective terms of the transport equations. We have verified the accuracy and reliability of the hybrid differencing scheme, i.e. the axial and secondary velocity profiles were also obtained using the third-order QUICK scheme with similar results. The two differencing schemes also had little effect on particle motion and deposition patterns. Both relative differences in velocity magnitudes and particle deposition efficiencies were less than 10%. The sets of linearized and discretized equations for all variables were solved using an algebraic multi-grid method (Lonsdale 1993). The particle transport equations were also solved using the same commercial program in combination with user-specified drag correlations and detailed near-wall particle tracking. In CFX, the equations for particle trajectories are solved numerically using Gear's BDF method. After each iteration for each particle, the information about position, time, and three components of the velocity as well as the speed with which the particles cross the control volume boundaries was obtained. The user-specified near-wall particle tracking program was used to calculate the distances from the centre of particles to the wall and then record if the particles deposit.

A dimensionless approach was adopted for the simulation of the conservation equations. The mean inlet fluid velocity, U, along with the fluid density, ρ, were set equal to one, and the absolute fluid viscosity, μ, was adjusted to achieve the desired fluid Reynolds number based on inlet tube diameter D_1, $Re_{D_1} = (\rho D_1 U)/\mu$. Likewise, the particle Stokes number, $St_{D_1} = (\rho_p d_p^2 U)/(18\mu D_1)$, based on the inlet tube, was specified by adjusting the particle density, ρ_p, for a given particle diameter, d_p, and the previously defined fluid flow field settings (see table 1). Based on the symmetry assumptions and the parabolic inlet profile, the particles simulated in this analysis had a parabolic distribution across 1/4 of the bifurcation inlet (1/2 model inlet; see figure 1*a*). In the current models the number of particles, i.e. $n = 1839$ for one-quarter plane, was determined by increasing the inlet particle concentration until deposition efficiency became independent of the number of particles simulated. The deposition efficiency, η, was defined as the ratio of the number of particles deposited in a given region to the total number entering the region.

As stated in Part 1, the mesh was generated based on the surface information obtained from Pro/Engineer models of the experimental glass tube bifurcations. Utilizing the assumed symmetry condition about the first bifurcation plane, the flow field simulation involved only the upper half of the bifurcation model (i.e. $z \geqslant 0$). The inlet and outlet locations, and the mesh topology were determined by refining the mesh until grid independence of the flow field solution and particle deposition efficiency was achieved. The final mesh size of the planar and 90° non-planar configurations was 161 000 and 173 000 cells, respectively. The computations were performed on a Sun Ultra 60 workstation with 512 MB of RAM with two 300 MHz CPUs. The steady-state solution of the flow field was assumed converged when the dimensionless mass residual, (total mass residual)/(mass flow rate) $< 10^{-3}$. A typical run time for the fluid flow simulations on a single processor was approximately 2.7 hours. Utilizing the converged flow field solution, the particle trajectory simulations required approximately 16 minutes for each Stokes number simulated.

3. Results and discussion

3.1. *Model validation*

The computational fluid–particle model has been validated with experimental velocity data of Zhao & Lieber (1994) in Part 1. In Comer *et al.* (2000), measured aerosol deposition efficiencies, $\eta = \eta(St)$, as a function of the Stokes number, $0.02 \leqslant St \leqslant 0.25$, were compared with the computer predictions for double-bifurcation glass tube models, i.e. planar and non-planar configurations (Kim & Fisher 1999). An excellent agreement was achieved between experimental $\eta(St)$-values and computational data points for the first and second bifurcations of either configuration. Other experimental validations of the present fluid–particle computer simulation code may be found in Comer *et al.* (1998) or Comer (1998). The good comparison between experiment and theory instils confidence that the computer simulation model is sufficiently accurate and flexible to analyse fluid–particle dynamics in multi-generation lung model segments.

3.2. *Particle dynamics*

Three-dimensional particle dynamics in highly vortical flows are best visualized in animated form using appropriate software and video or CD-R recordings because of the complexities in flow structure, particle trajectories and particle deposition patterns. Alternatively, snapshots of the Lagrangian time evolution of a volumetric particle input pulse, selected particle trajectories, cross-sectional particle distributions, and particle deposition patterns are useful to elucidate basic physical insight. For all particle dynamics results rounded carinal ridges, i.e. $r/D = 0.1$ where r is the radius of the nose of the flow divider and D the diameter of the daughter branch, were assumed, except in the last section where $r/D \approx 0$ (see figures 18 and 19).

3.2.1. *History of particle deposition patterns*

In order to illustrate the connection between particle inlet conditions and the resulting deposition patterns, the start positions of all particles which deposit within the double bifurcation are identified (see figures 2 and 3) and the dispersion of a volumetric particle input pulse, a total of 73 560 spheres, is recorded (see figure 4*a–h*, where $\tau = tU/D$). Selected particle trajectories are depicted in figure 5, demonstrating for the planar configuration ($Re_{D_1} = 2000$, $St_{D_1} = 0.12$, and $d_p = 5\,\mu\text{m}$) direct impaction onto the carinal ridges, wall deposition due to three-dimensional vortical flow effects, and unhindered sweeps through the branching tubes. Specifically, figures 2 and 3 indicate that for a given Reynolds number and configuration, the inlet regions from which particles deposit increase with higher Stokes numbers but retain their basic shapes. Deposition in the first bifurcation is generally unaffected by the orientation of the second bifurcation (compare figure 3 to figure 2), where the distance between the cut-off point defining geometric transition zone from the first to second bifurcation and the first flow divider is 0.6 cm (see figure 2 in Part 1). Most particles deposit through inertial impaction at the first carina, as shown with the vertical shape of particle release positions for the first bifurcation in figures 2 and 3. At $Re_{D_1} = 2000$, the central particle capture region, i.e. along the z-axis, is extended upward. The additional particles impact away from the carina due to secondary flows. For the planar configuration, a small particle capture region, i.e. somewhat parallel to the y-axis, changes its tail-end direction at $Re_{D_1} = 2000$ at all Stokes numbers. Again, particles starting in these locations experience strong vortical flows at high Reynolds numbers (see figure 2). For the non-planar model, particles which deposit along the

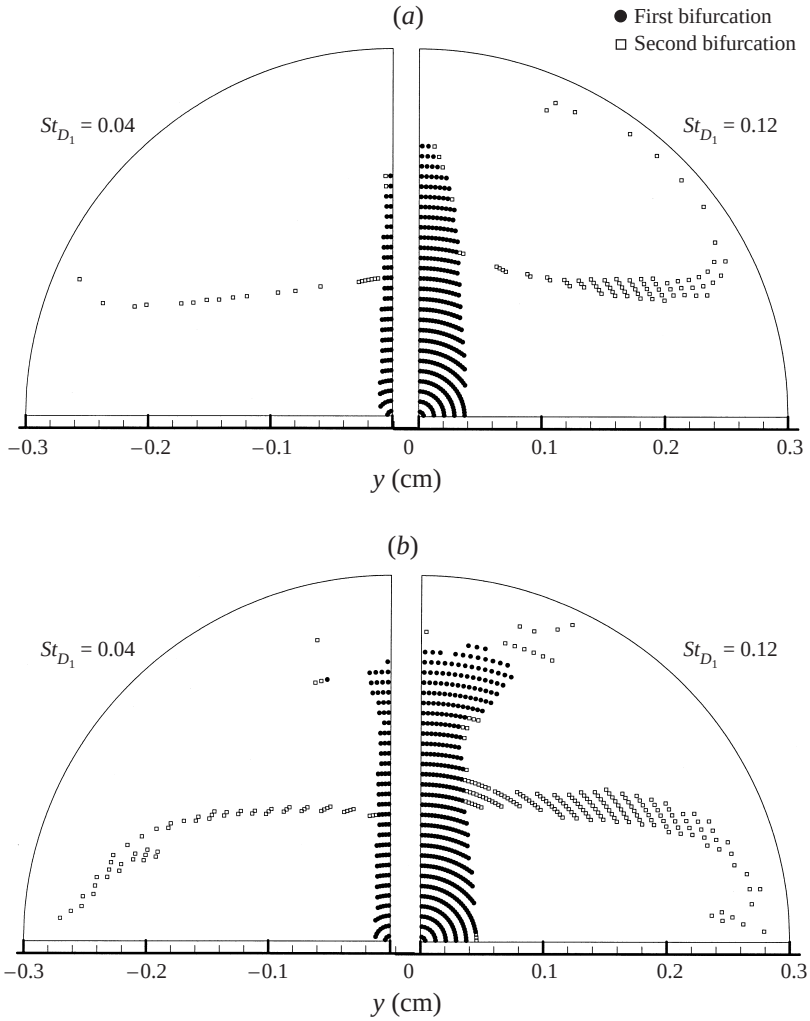

FIGURE 2. Inlet release positions of depositing particles in the planar configuration: (*a*) for Re_{D_1} = 500 and (*b*) for $Re_{D_1} = 2000$; $St_{D_1} = 0.04$ and 0.12. Number of particles (quarter inlet) = 1839.

inside portion of the second bifurcation were released from positions along the y-axis. In contrast, particles which deposit primarily along the outside portion of the bifurcation originated from a region along the z-axis (see figure 3). In order to show the transients and to demonstrate that the deposition patterns are not dependent on the inlet particle distribution but on the release positions, a finite volume of uniformly distributed particles, i.e. a 'particle pulse' has been swept through the planar model (see figure 4*a*) and tracked in the dimensionless Lagrangian time frame, $\tau = t\,U/D$ (figure 4*b–e*). The volumetric particle pulse is equivalent to the release of a series of aerosols from the inlet plane at different times, i.e. forming a particle cloud. The volumetric particle pulse impacts on the first carinal ridge and divides symmetrically until the second bifurcation (figure 4*b*, *c*). The asymmetric split of the particle suspension stream around the second bifurcation is clearly depicted in figures 4(*d*) and 4(*e*). After about $\tau \geqslant 20$, quasi-equilibrium deposition patterns have been formed (see figure 4*f*). While in figure 4 all 73 560 particles are projected onto a surface normal

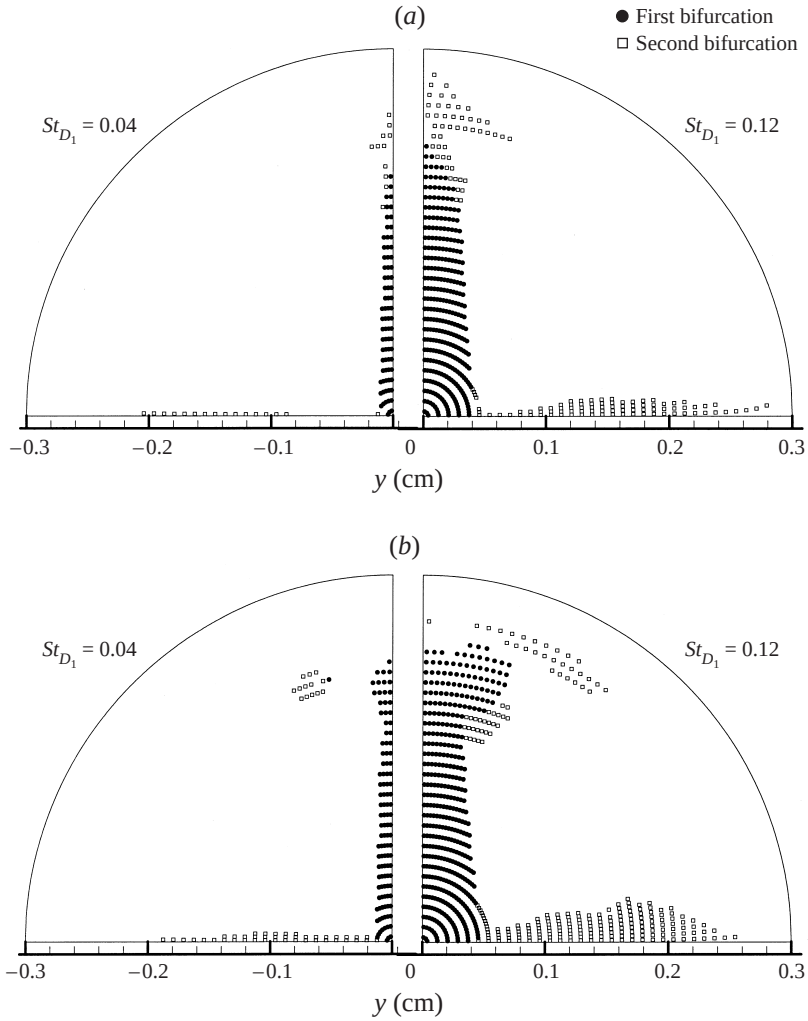

FIGURE 3. As figure 2 but in the non-planar configuration.

to the observer, figure 5 shows the inlet positions and trajectories of 26 individual particles ($d_p = 5\,\mu$m, $Re_{D_1} = 2000$, $St_{D_1} = 0.12$). Of the four centre particles (symbol c is marked on their trajectory lines), two near the z-axis impact onto the carinal ridge, whereas the other two are deflected and move out of the system. The string of particles forming an arc in the first quadrant of the release plane bypass the first carina but then deposit on the second ridge and sidewall of the daughter tube or migrate out of the double bifurcation. Near-wall release does not necessarily imply surface deposition, as shown with a single particle in the first quadrant and four particles starting in the second quadrant. The trajectories of these five particles indicate the strong influence of the local vortical flow patterns discussed in Part 1.

Particle distributions and flow directions at different cross-sections (see figure 1b) are shown in figures 6–9. Specifically, the influence of the velocity field in conjunction with particle inertia effects is shown in figures 6 to 8 for the planar configuration and in figure 9 for the non-planar configuration, both for $Re_{D_1} = 500$ and 2000 with $St_{D_1} = 0.12$ and $d_p = 5\,\mu$m. The particle motion in one section was captured just

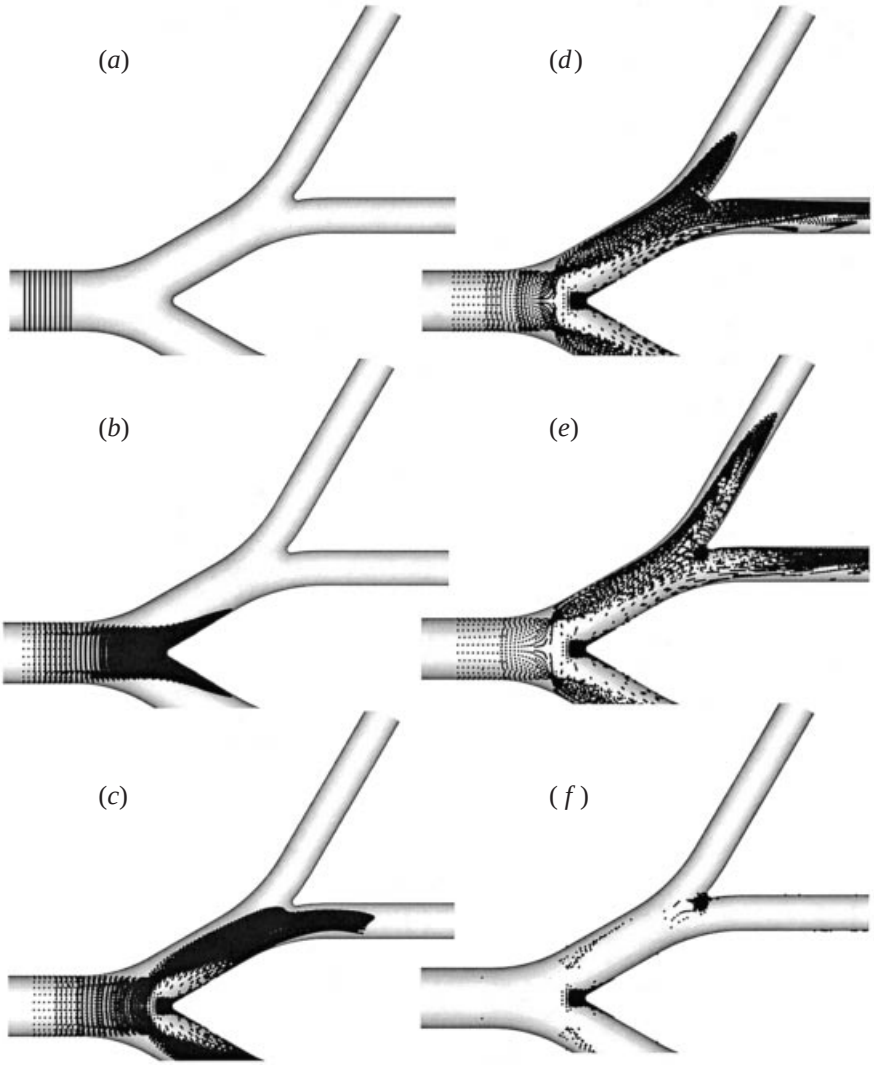

FIGURE 4. Time evolution of volumetric particle pulse: (*a*) the start at $\tau = 0$; (*b*) $\tau = 1$; (*c*) $\tau = 2$; (*d*) $\tau = 3$; (*e*) $\tau = 4$; and (*f*) final deposition pattern.

when these particles passed through this cross-section. The desired Stokes number for a specified Reynolds number was obtained by changing the particle density (see table 1). These cross-sectional particle distributions plus directional indicators should be viewed with the corresponding velocity vector plots of Part 1 in § 3.2. The cross-section locations are selected to exhibit the particle motions in slices C–C′, F–F′, and H–H′ in Part 1, which are also denoted in figure 1(*b*). At low Reynolds numbers (e.g. $Re_{D_1} = 500$), the strength of the secondary flow is weaker than that in the high Reynolds numbers case, i.e. the particles can generally follow the axial motion even for somewhat high Stokes numbers, e.g. $St_{D_1} = 0.12$. For high Reynolds numbers, the intensity of secondary velocity or vortical flow becomes strong, i.e. particles may be pulled away from the vortex centres, generating distinct particle-free zones in the tube's central region and unique particle deposition sites other than the carinas (see

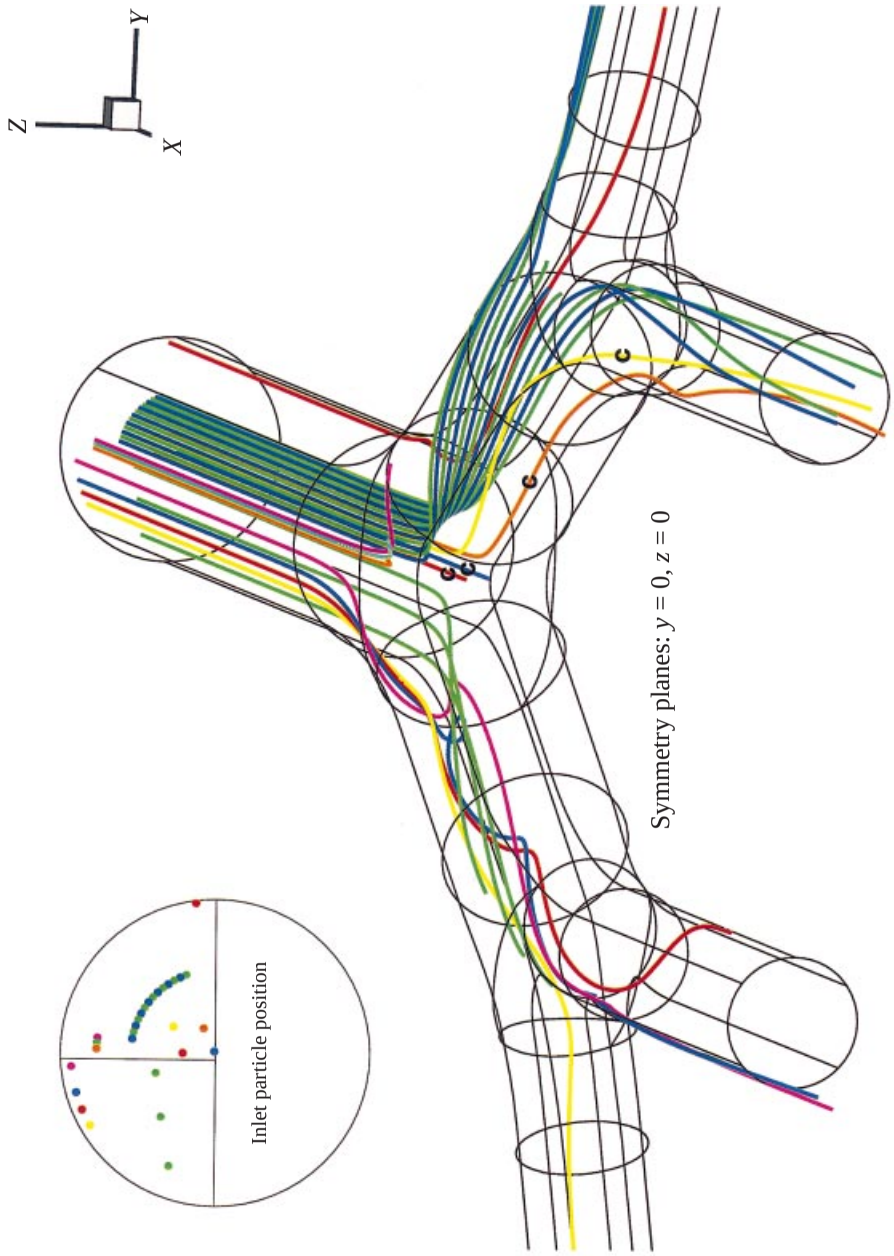

FIGURE 5. Selected particle release positions and airway trajectories.

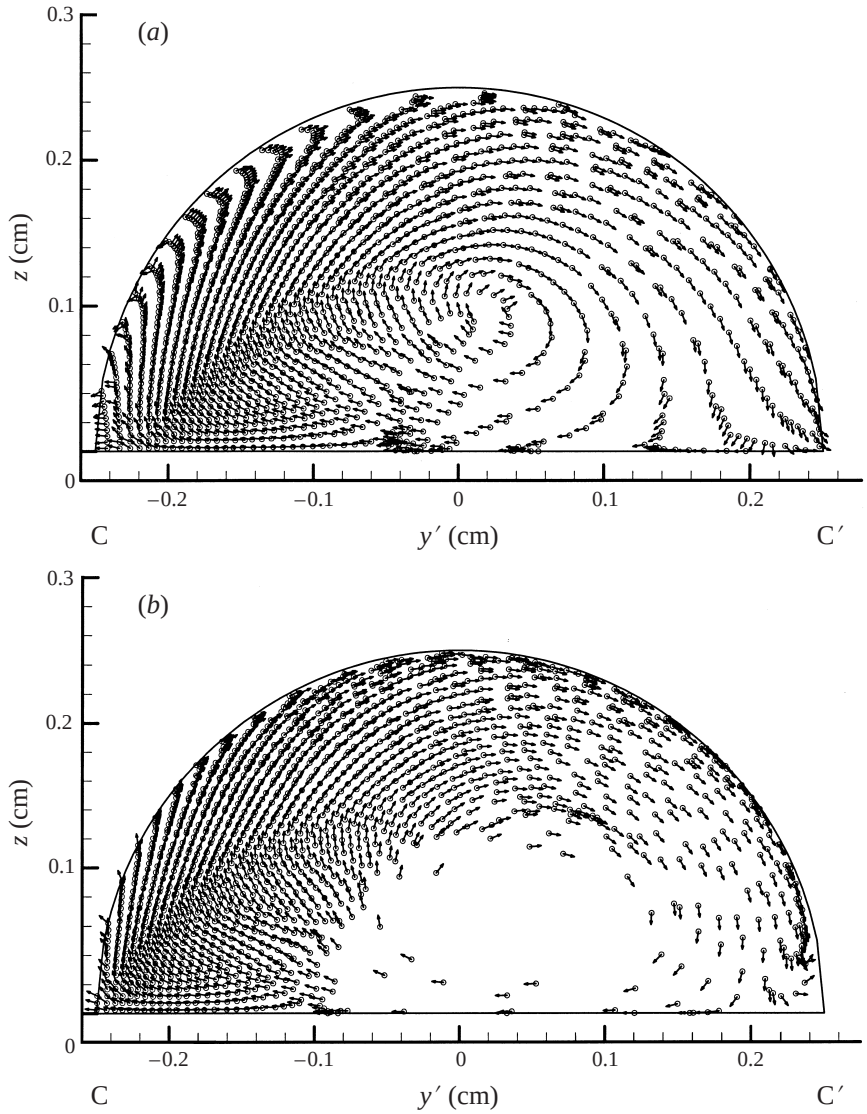

FIGURE 6. Particle distributions and flow directions in the planar bifurcation at cross-section C–C′ for: (*a*) $Re_{D_1} = 500$ and (*b*) $Re_{D_1} = 2000$; $St_{D_1} = 0.12$. (The arrow only indicates the direction of particle motion.)

figure 6*b* for cross-section C–C′). Thus, the dense particles cannot follow the curved secondary streamlines and instead spiral away from the centre of the vortex. This vortex effect for relatively high Reynolds numbers is present even for the lowest Stokes numbers (e.g. $St_{D_1} = 0.02$), but is more pronounced at the higher Stokes numbers (e.g. $St_{D_1} = 0.12$). In general, with an increase in Stokes number, the radial force on these heavy particles increases, which enlarges the particle void regions, and the particle concentrations along the outside of the vortex (i.e. the convergence zone) become larger. However, the basic characteristic of particle motion do not vary much in a Stokes number range of $0.02 \leqslant St_{D_1} \leqslant 0.12$ at a fixed Reynolds number. Thus, the following discussion will be limited to $St_{D_1} = 0.12$ at Reynolds numbers of $Re_{D_1} = 500$

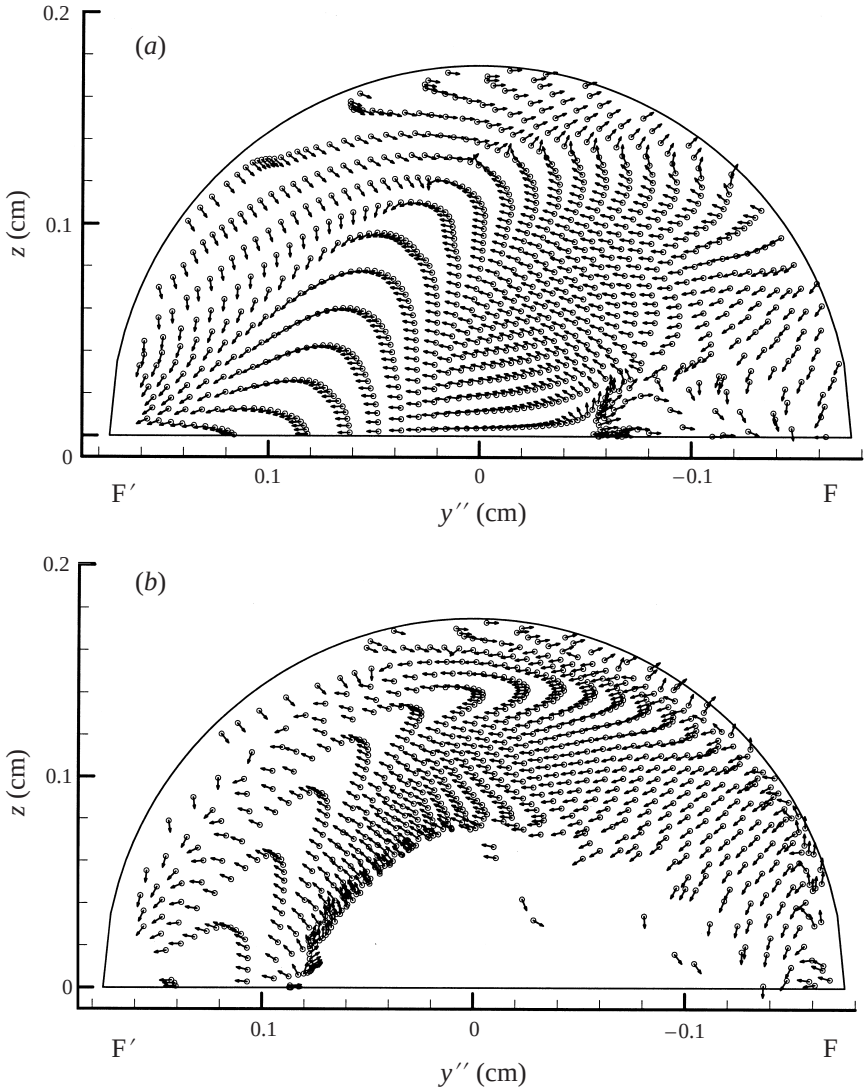

FIGURE 7. As figure 6 but at cross-section F–F′.

and 2000. In addition, the local changes in particle concentration are a function not just of the local vorticity but of the entire vortex field through which the particles have passed. It is a cumulative effect. With the change of the cross-section in the same tube, the particle-free zone varies slightly. The preferential concentration of particles caused by the coherent vortical structures was also demonstrated in experimental and numerical studies for turbulent flows, as reviewed by Eaton & Fessler (1994).

Figure 7(*a*, *b*) depicts the particle distributions and directions in the inside tube after the second bifurcation (see cross-section F–F′ in figure 1*b*). Again, for the low Reynolds number case we see that the flow field, specifically the axial flow field, is a good indicator of the particle concentration. This follows from the fact that the secondary flow is considerably weaker. Of interest is the region where two counter-rotating vortices meet; as a result, the combined centrifugal force generates a higher local particle concentration. For the $Re_{D_1} = 2000$ case, the high-flow region

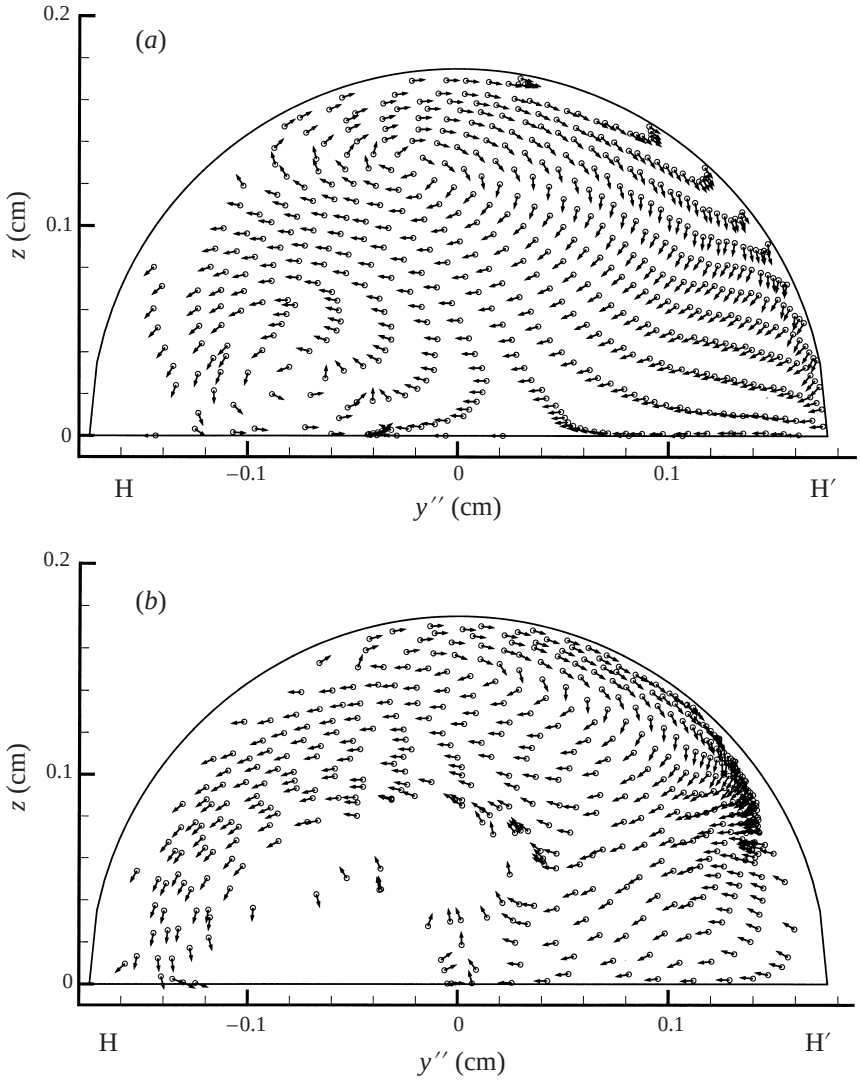

FIGURE 8. As figure 6 but at cross-section H–H′.

has wrapped further around the top and a larger low-flow region exists on the outside of the second bifurcation tube while the higher-flow region is nearer the inside wall of the second bifurcation. The particle concentration again appears to be somewhat related to the flow rate; however, the large void region in the centre of the tube is again present. This can be attributed to the strong vortex, as previously discussed. Thus, the highest particle concentration is generally along the outside of the vortex. At cross-sections downstream of F–F′, the situation is essentially the same at $Re_{D_1} = 500$ because the secondary flow is very small. In the $Re_{D_1} = 2000$ case, the high-flow region wraps even further around the top of the daughter tube and the vortex centre shifts toward the outside of the second bifurcation tube downstream of cross-section F–F′. This results in the void region being shifted toward the outside of the tube.

For cross-section H–H′ in figures 8(*a*) and 8(*b*), the particle flow fields differ measurably from figure 7(*a*, *b*). Two distinct vortex regions appear due to the secondary

flow, although from the flow field plots it could be deduced that these secondary flow effects are weak (see figure 8*a*). Nevertheless, it can be argued that weaker secondary vortex flows acting over a longer time period at low axial velocities have a similar effect as stronger secondary vortices over a shorter time interval. Unlike for the inside tube (see figure 7), the flow rate does not provide an indication of the particle concentration. For this case, the particle concentration appears to be essentially uniform, with slightly higher concentrations existing at the outside of the tube and a region of very low concentration immediately adjacent to the inside wall. Apparently, the upstream carina effect initially forces the flow away from the divider (i.e. the inside wall) and toward the outside wall. This also helps to explain why there is a higher concentration on the outside of the tube for $Re_{D_1} = 2000$ (figure 8). Again, figure 8(*b*) shows a void region corresponding to the centre of the relatively strong vortex. Of interest is that the high concentration of particles located on the outside wall for the high Reynolds number case resides in a region of very low secondary flow where the particles are being convected downstream without moving laterally. This would definitely have an effect on particle deposition at any additional bifurcations downstream. The relationship between velocity and particle flow fields downstream of the slice H–H′ in the outside tube of the second daughter tube is essentially the same as that discussed for the cross-section H–H′, which follows from the fact that the secondary flow is very small for this case. For $Re_{D_1} = 2000$, the void zone is shifted toward the centre of the tube as well.

The cross-sectional particle distributions in the non-planar configuration start to differ after the second bifurcation (see figure 9*a*, *b*). So only the particle motion in slices H–H′ is displayed for the non-planar case. As discussed for the planar configuration, it is reasonable to assume, for the Stokes numbers considered, that the highest-flow-rate regions correspond to the highest particle concentrations. However, owing to the stronger secondary flows generated at the carina, this is not the case for the non-planar orientation.

For $Re_{D_1} = 500$ at station H–H′, the highest particle concentration is located along the $(-y')$ side of the second daughter tube which corresponds to the side of the first daughter tube with the highest particle concentration. Owing to the relatively small secondary flow no significant difference is seen in the particle distribution between stations H–H′ and downstream stations, because the particles are essentially convected downstream.

For the case of high Reynolds number flow at cross-section H–H′, the secondary flow is significant, and two counter-rotating vortices generate two regions void of particles (figure 9*b*). Specifically, the regions at the inside (i.e. bottom) of the second bifurcation $(-z')$ where the particles are being pulled around the daughter tube, correspond to a region of localized deposition discussed in the next section. This also supports the previous statement which suggested that there is little relationship between the fluid flow rate and the particle concentration in the non-planar daughter tube.

3.2.2. *Local particle depositions*

Health effects of inhaled aerosols in the human lung not only depend on the overall particle deposition efficiencies for a given airway tract, but also on the local wall particle concentrations (Schlesinger & Lippmann 1978). Figures 10–17 depict the particle depositions on the wall surface for both the planar and non-planar configurations at representative Stokes and Reynolds number values, i.e. $St_{D_1} = 0.04$ and 0.12 and $Re_{D_1} = 500$ and 2000 from various perspectives: (*a*) the symmetry plane

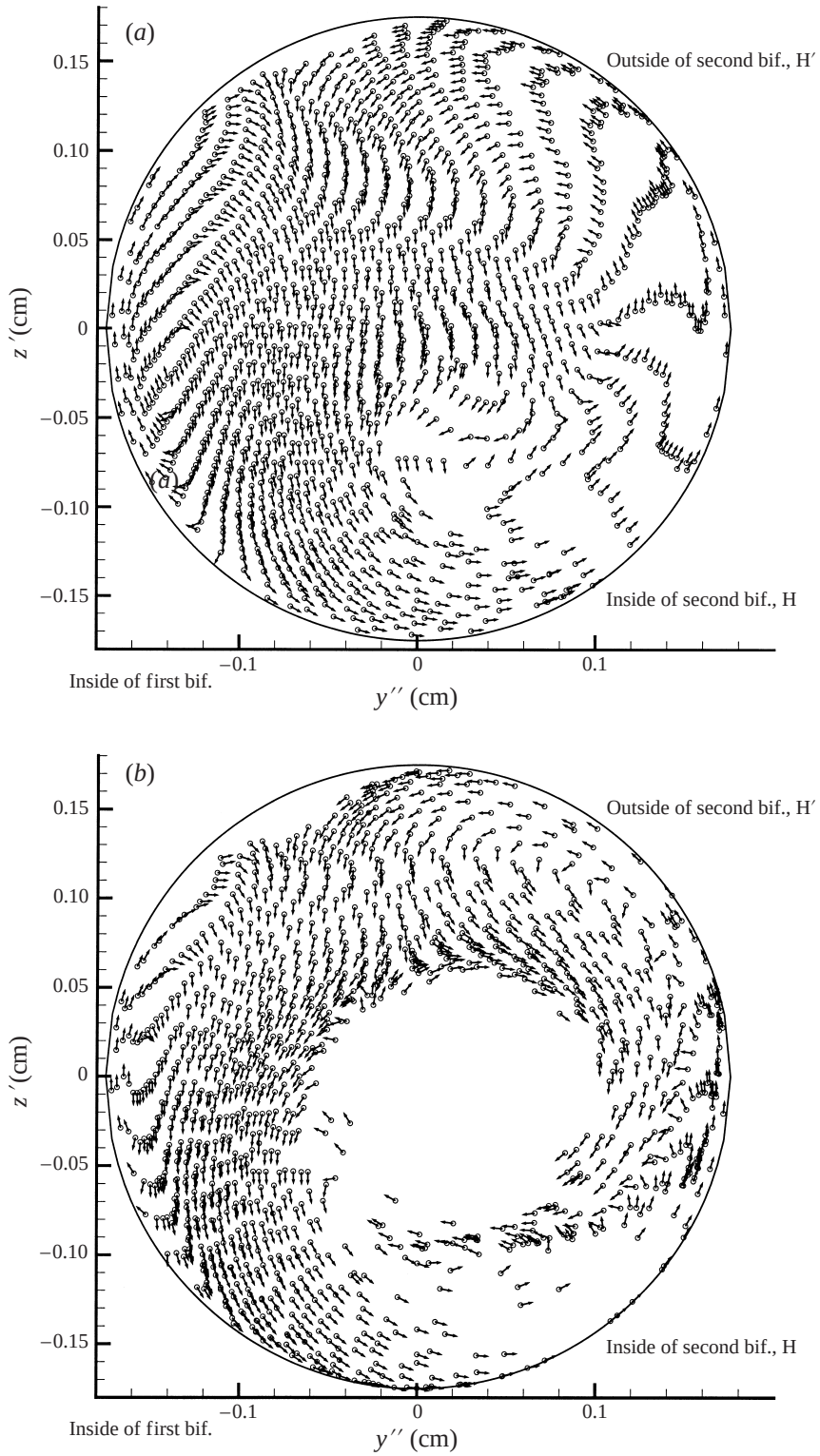

FIGURE 9. Particle distributions and flow directions in the non-planar bifurcation at cross-section H–H′ for: (*a*) $Re_{D_1} = 500$ and (*b*) $Re_{D_1} = 2000$; $St_{D_1} = 0.12$. (The arrow only indicates the direction of particle motion.)

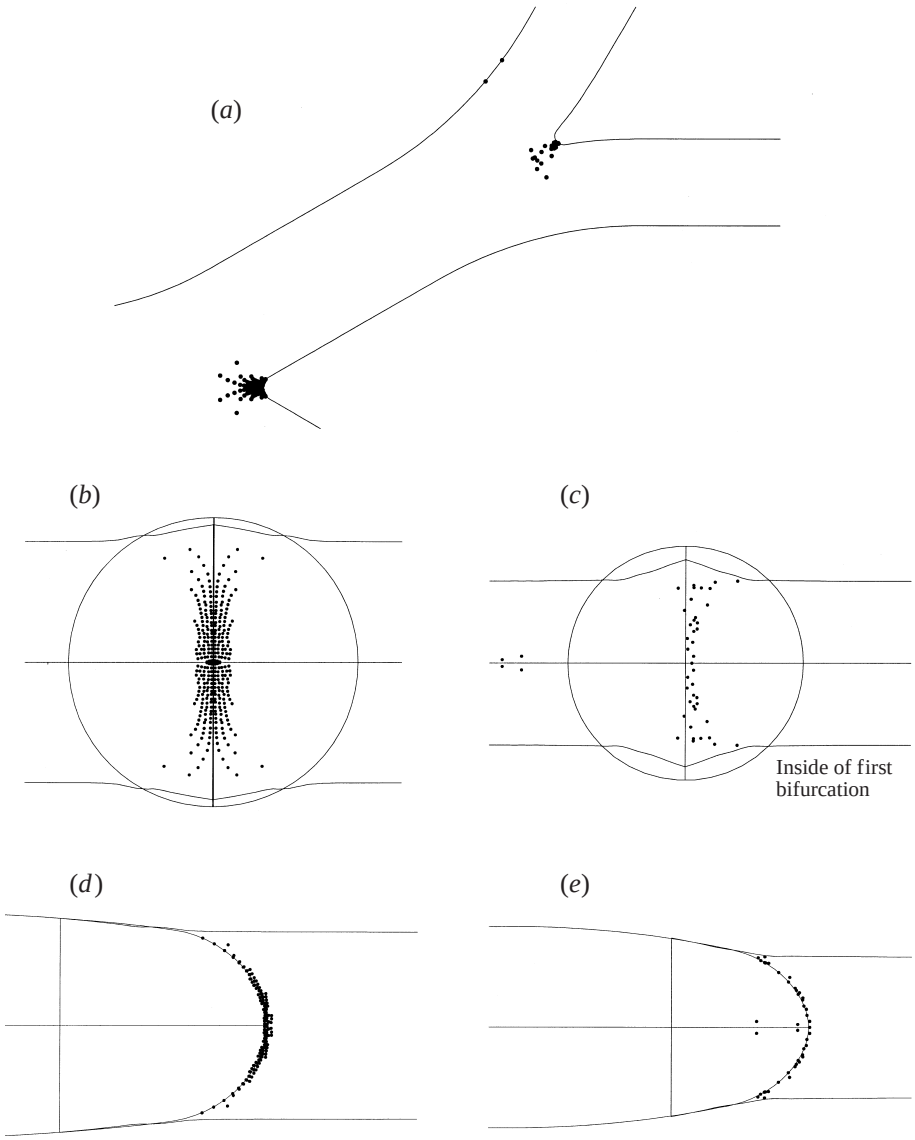

FIGURE 10. Various views of local particle deposition patterns in the planar configuration at $Re_{D_1} = 500$ and $St_{D_1} = 0.04$: (*a*) planar view $z = 0$; (*b*) upstream view of first carinal ridge; (*c*) upstream view of second carinal ridge; (*d*) side view of first bifurcation; and (*e*) side view of second bifurcation.

($z = 0$); (*b*) and (*c*) the first and second bifurcation inlets; and (*d*) and (*e*) the first and second bifurcation side views for both planar and non-planar configurations. As discussed in Part 1, the incoming flow splits at the stagnation point (i.e. first divider), hugs the inside wall of the first daughter tube, D_2, and generates a weak recirculation zone along the outer wall as well as a symmetric pair of vortices perpendicular to the axial flow. This complex vortical flow is split again at the second divider, resulting in slower but highly three-dimensional velocity fields in the second pair of daughter tubes, D_3. At this juncture it is interesting to note that several researchers (Zhao & Lieber 1994; Zhao, Brunskill & Lieber 1997; Farag *et al.* 1998) have reported

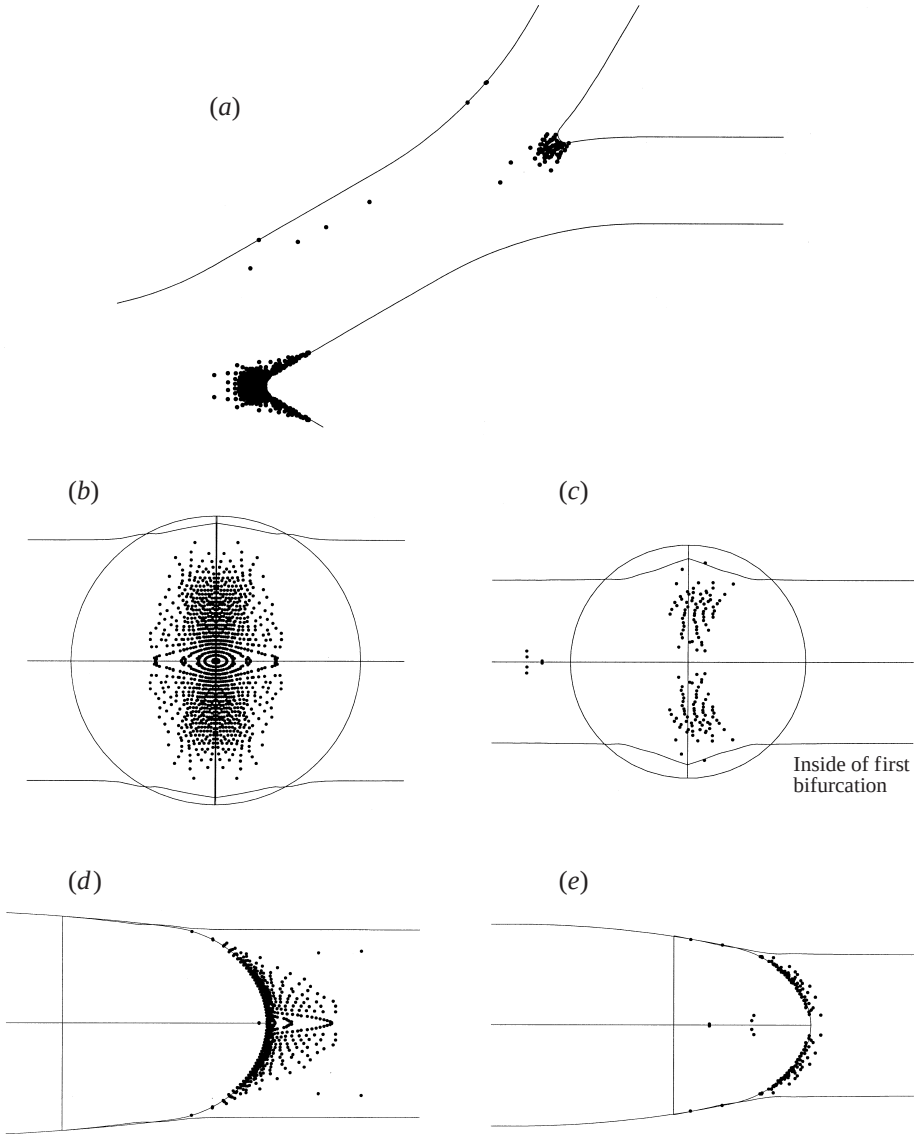

FIGURE 11. As figure 10 but at $Re_{D_1} = 500$ and $St_{D_1} = 0.12$.

that flow separation does not occur in symmetric three-dimensional bifurcating lung models. Flow separation was observed in the present study (see Part 1) and this discrepancy is due to differences in the geometric shape of the geometric transition regions, which in the current study are more faithfully duplicated by using the glass tube model of Kim & Fisher (1999). In general, particle deposition occurs primarily due to direct impaction at the stagnation points (i.e. carinal ridges) and hence the higher Stokes and Reynolds number cases correspond to higher depositions. At the first bifurcation, particles are concentrated symmetrically along the carinal ridge with the highest concentration in the central portion of the carina. For $Re_{D_1} = 500$ but at the higher Stokes number, the particle deposition increases, as previously discussed, and the deposition efficiency again increases; however, the deposition pattern is spread

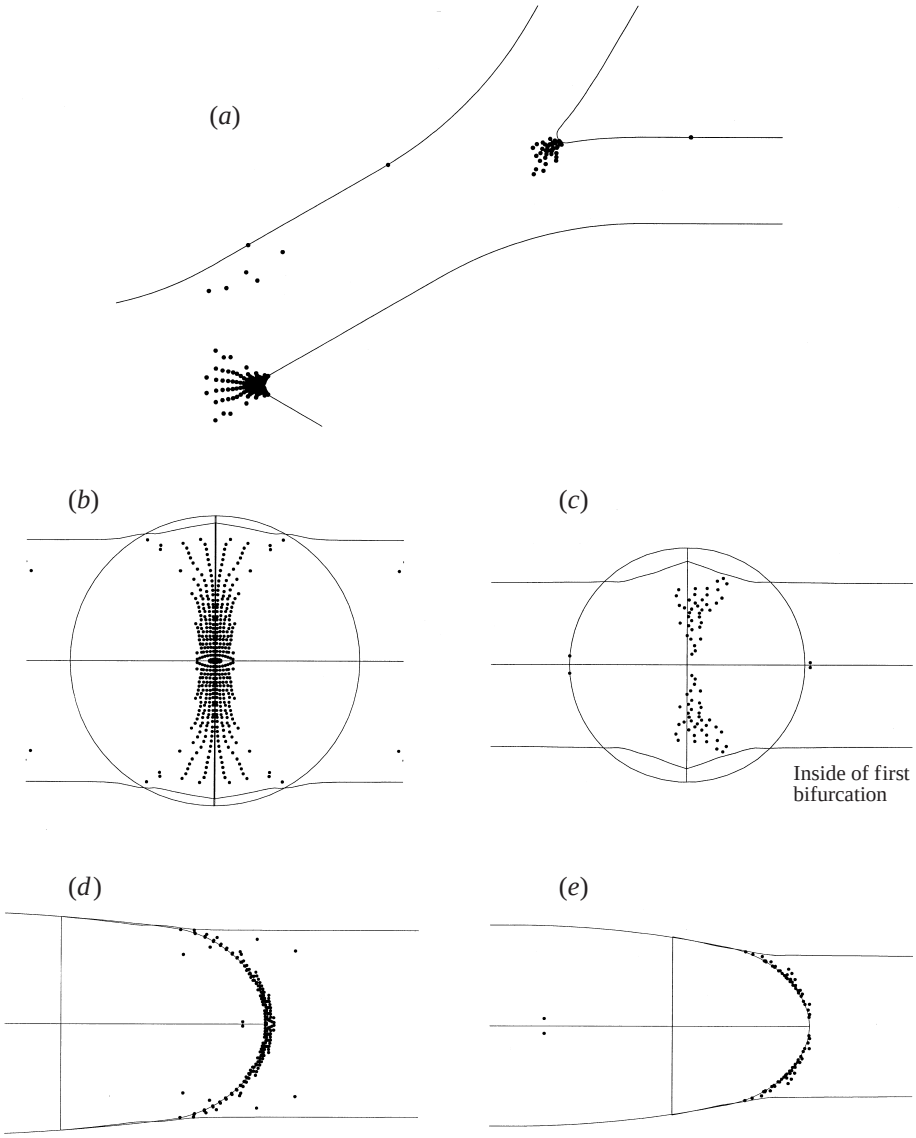

FIGURE 12. As figure 10 but at $Re_{D_1} = 2000$ and $St_{D_1} = 0.04$.

over a much larger surface area due to the higher secondary motion. The particle concentration at the second bifurcation is considerably lower than that at the first one, and the symmetry in particle deposition about the carina is not repeated because of the highly disturbed flow fields in the first daughter tubes.

For the planar configuration figures 10 to 13 show that a larger number of particles deposit on the high-flow side of the second carina and that a region of low particle concentration exists in the carinal centre. The second observation can be attributed to the lower axial velocity in the vicinity of the second carina. This effect is enhanced at higher Reynolds numbers. At the higher Reynolds number, a recirculation zone exists immediately upstream of the carina. This has the effect of creating a 'blockage' to the main flow, guiding it smoothly into the daughter tubes and away from the

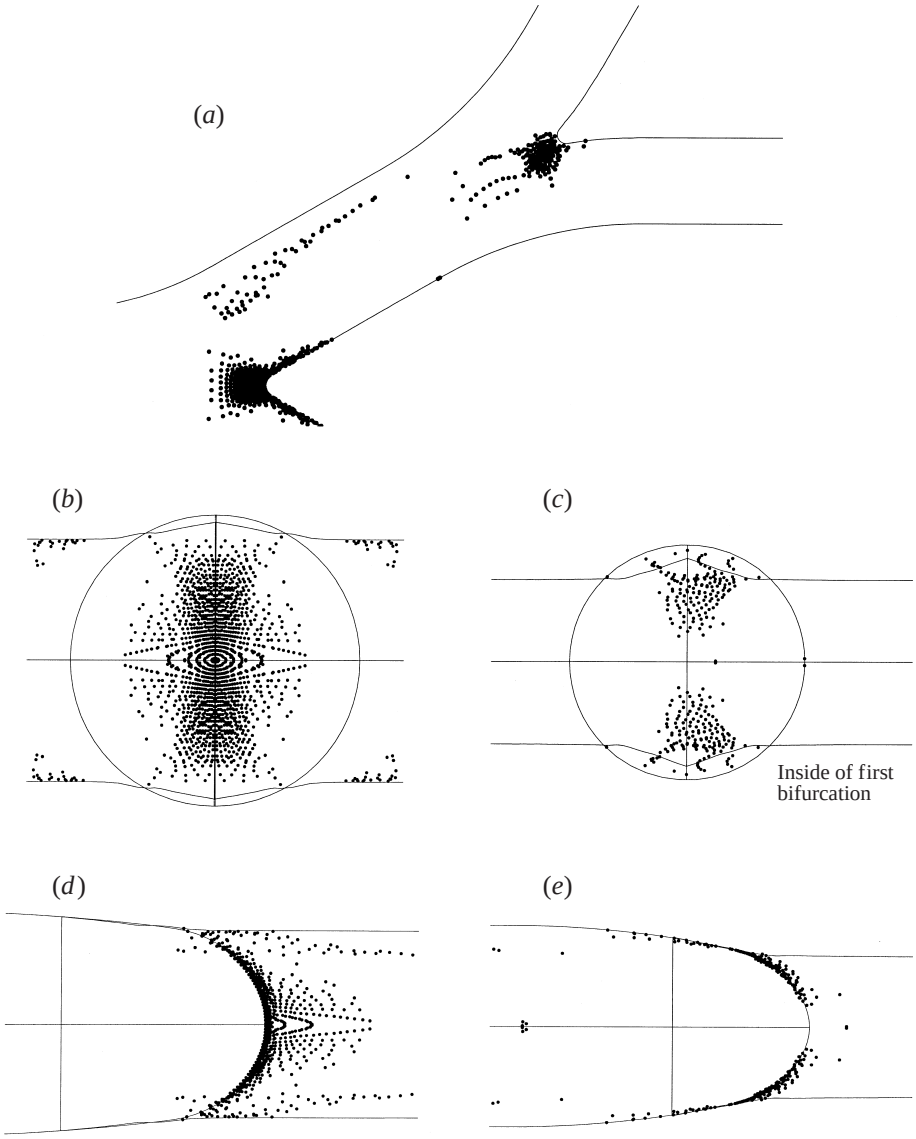

FIGURE 13. As figure 10 but at $Re_{D_1} = 2000$ and $St_{D_1} = 0.12$.

divider wall. At higher Stokes numbers, the particle concentration in the central carinal region is lower than at low Stokes numbers for a given Reynolds number. This can be attributed to the fact that the flow is guided along the carinal ridge and hence the axial flow deflects away from the divider. At higher Stokes numbers the particles moving with the flow along the curved carinal ridge deposit prior to reaching the central portion of the carina.

The 90° turn of the second pair of daughter tubes in the non-planar configuration (see Part 1) produces very different particle deposition pattern in the second bifurcation area (see figures 14 to 17). Most particles impact asymmetrically at the ridge while the rest land along the sidewalls due to local secondary flows, described in § 3.2 of Part 1.

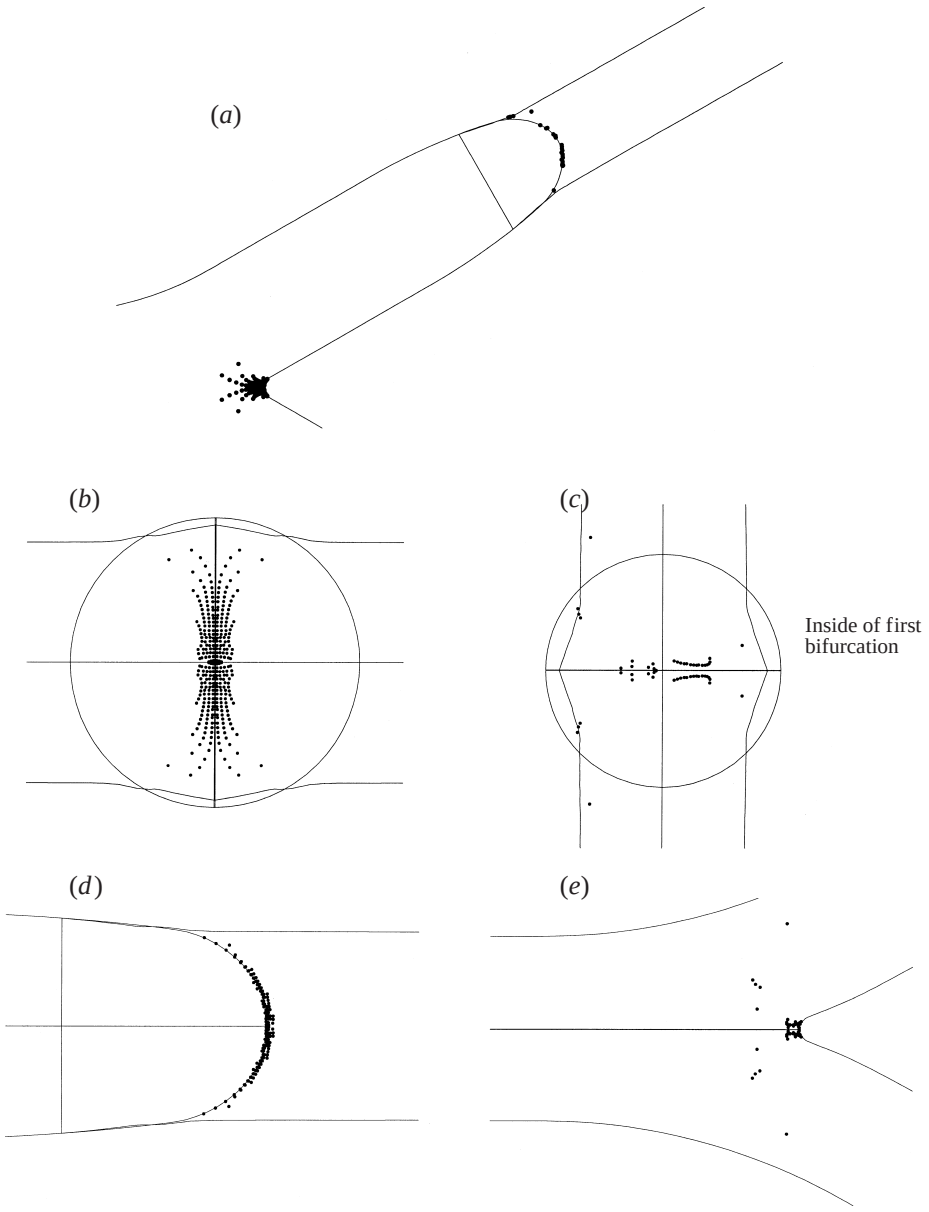

FIGURE 14. Various views of local particle deposition patterns in the non-planar configuration at $Re_{D_1} = 500$ and $St_{D_1} = 0.04$: (*a*) planar view $z = 0$; (*b*) upstream view of first carinal ridge; (*c*) upstream view of second carinal ridge; (*d*) side view of first bifurcation; and (*e*) side view of second bifurcation.

Most of these effects are not predicted with the previous single bifurcation models, and the double-bifurcation experimental measurements to date (see Kim & Fisher 1999) only show the global deposition efficiencies. Thus, these computational results provide new insight into the causes of highly non-uniform particle surface concentrations which exist in multi-branching airways. As specific sites in the lungs are both more susceptible to injury and more responsive to drugs, this detailed knowledge

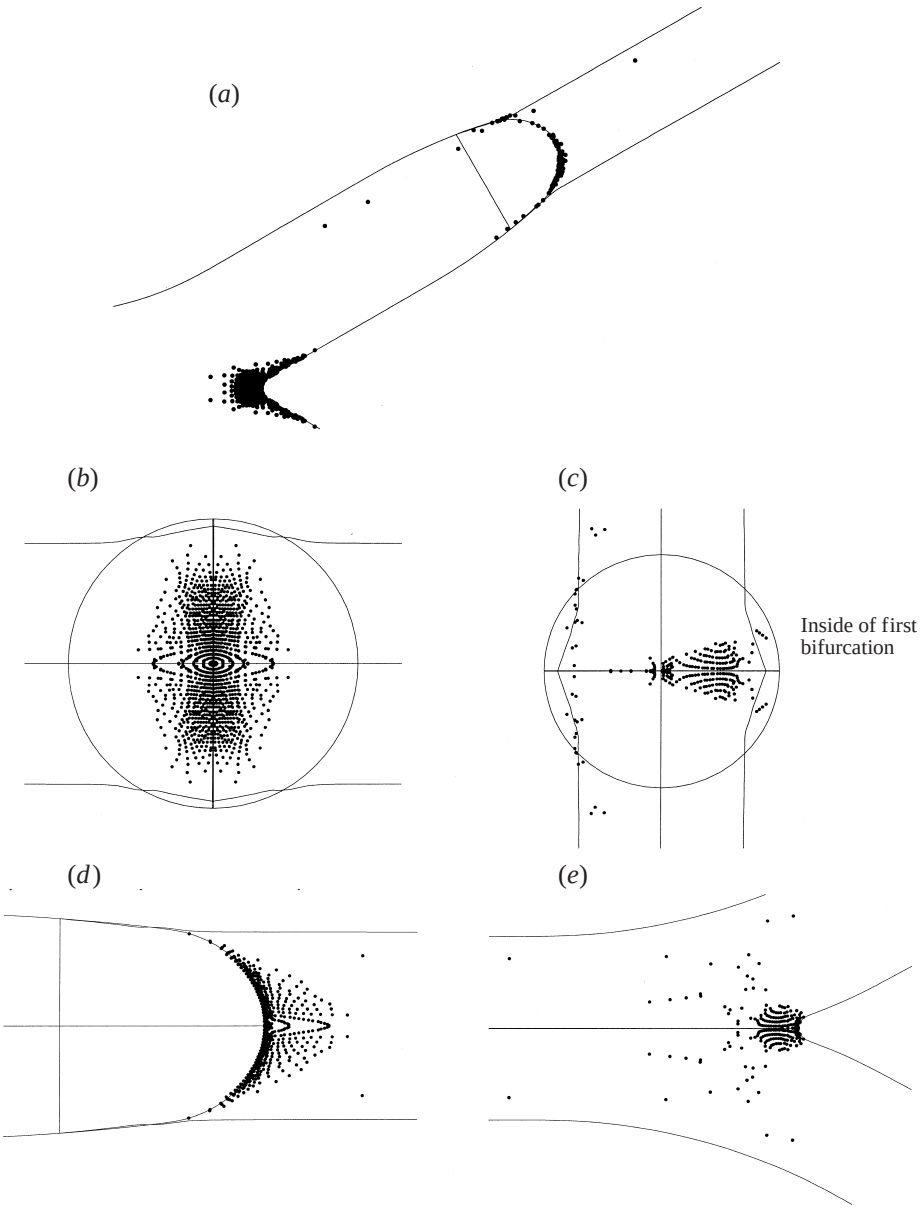

FIGURE 15. As figure 14 but at $Re_{D_1} = 500$ and $St_{D_1} = 0.12$.

should be of significant interest in both advanced health risk assessment and drug delivery protocol development (Dolovich 1993).

3.2.3. *Effect of the carinal ridge shape*

The above results and discussion focused on bifurcations with slightly rounded carinal ridges. As analysed in Part 1, the flow fields in the planar double bifurcation with both very sharp ($r/D = 0$) or slightly rounded ($r/D = 0.1$) carinal ridges were quite similar, with subtle differences in airflow structure in the vicinity of the carinal ridges. This also indicates that particle motions in the tubes of these two configurations

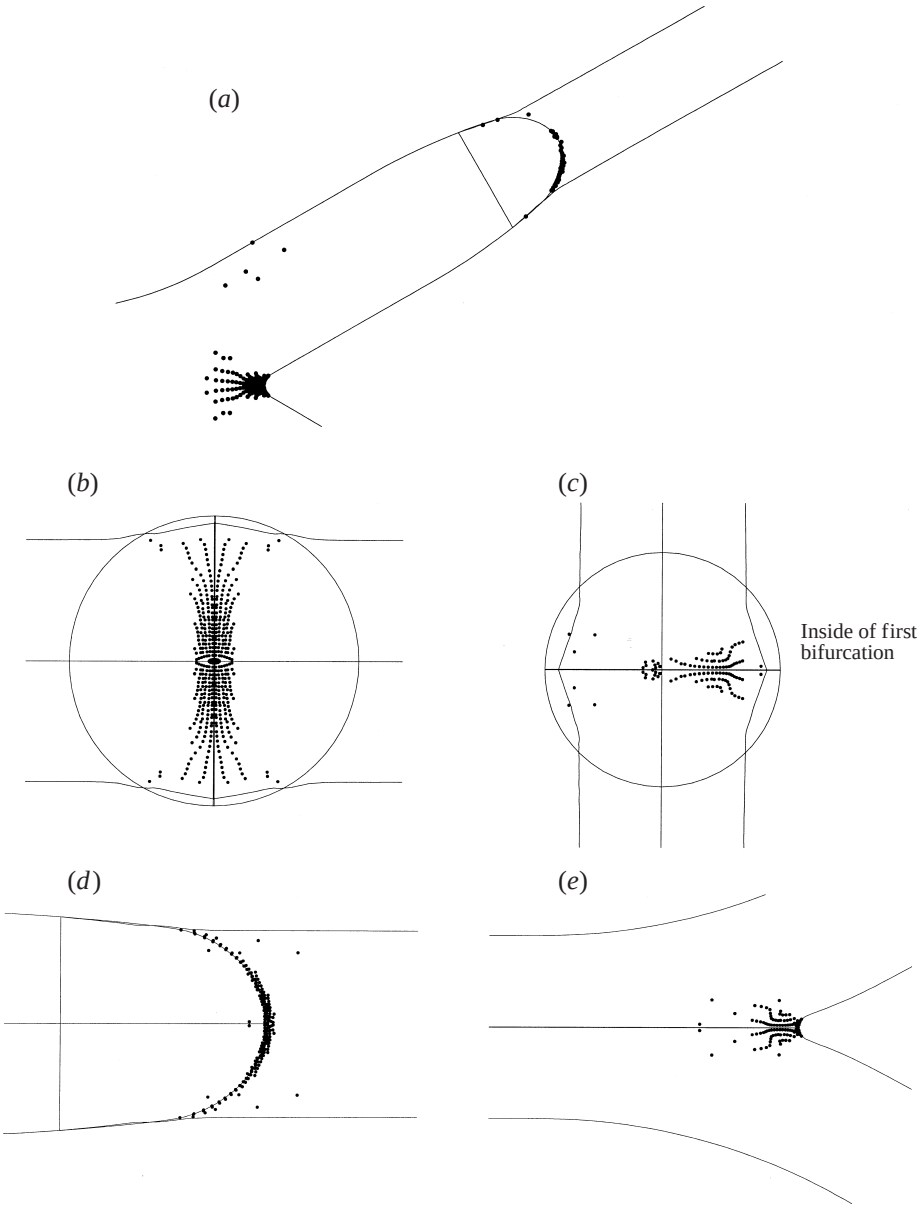

FIGURE 16. As figure 14 but at $Re_{D_1} = 2000$ and $St_{D_1} = 0.04$.

and hence their deposition efficiencies should not change much for a fixed Reynolds and Stokes number combination. Figure 18 shows the comparison between the deposition efficiencies (DE) for the double bifurcation with sharp vs. rounded carinal ridges for $Re_{D_1} = 500$ and 2000. It can be seen that the geometry factor has little effect on the DE for both Reynolds number cases. However, the local particle deposition patterns vary somewhat due to the geometric alteration (see figure 19 showing the mid-plane view for deposition patterns at $Re_{D_1} = 2000$ and $St_{D_1} = 0.12$). Specifically, more particles are deposited in the geometric transition zone upstream of the sharp flow dividers instead in the rounded carinas, especially in the second bifurcation. This

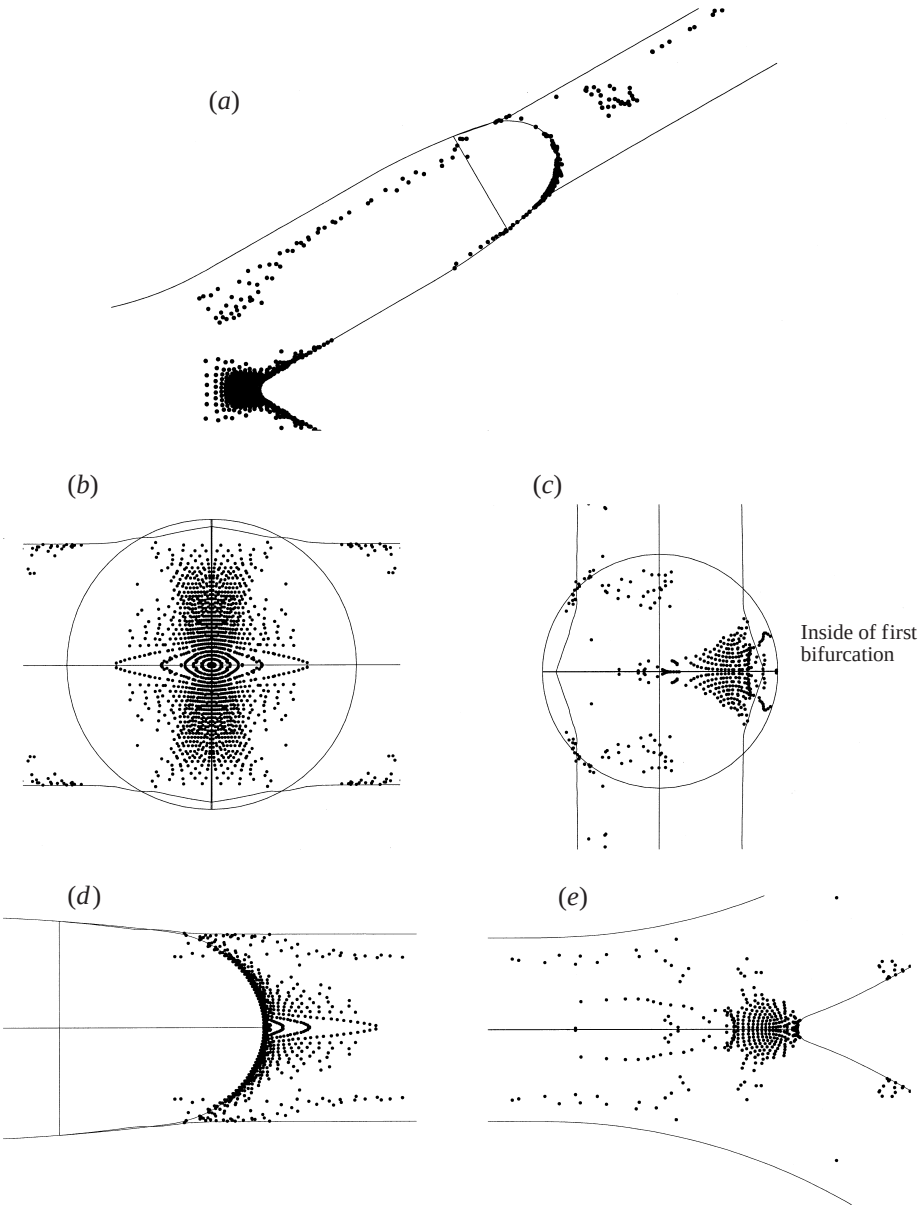

FIGURE 17. As figure 14 but at $Re_{D_1} = 2000$ and $St_{D_1} = 0.12$.

is because there exists a slightly extended (sharp) ridge where, due to the altered air flow, particles readily impact on the wall in the transition zone, i.e. the section which is more elliptical before the flow divider. Noting that the current double-bifurcation model with rounded carina is physiologically correct (see Part 1; Horsfield *et al.* 1971; Martonen, Yang & Xue 1994), the discussion on the particle motion and deposition should be a representative case for the bifurcating airway models. Also, the present methodology used for describing particle motions can be extended to other particle dynamics studies.

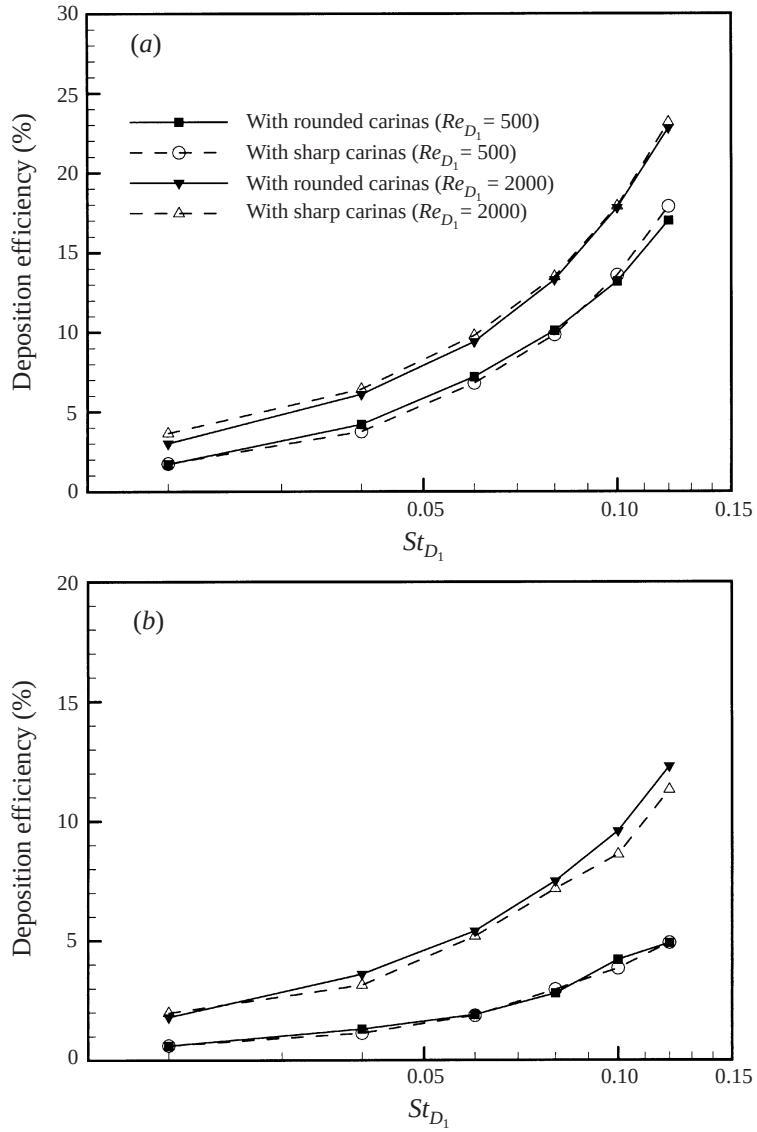

FIGURE 18. Comparison of deposition efficiencies for planar double bifurcations with rounded and sharp carinas at: (*a*) first bifurcation and (*b*) second bifurcation.

4. Conclusions

Health protection of susceptible population groups such as children and the elderly, as well as asthma suffers may benefit from more stringent air pollution standards which in turn have to be based on scientific methods. Experimentally validated computer analyses and predictions of aerosol deposition patterns in lung model segments are a cost-effective and useful tool to reach this goal. For the first-level analysis presented, it is assumed that the inhalation air flow is steady laminar and incompressible; the aerosols are spherical and non-interacting; the inlet Reynolds number range is $500 \leqslant Re_{D_1} \leqslant 2000$ and the Stokes number range is $0.02 \leqslant St_{D_1} \leqslant 0.12$; and the airways are rigid and smooth. While the overall percentage

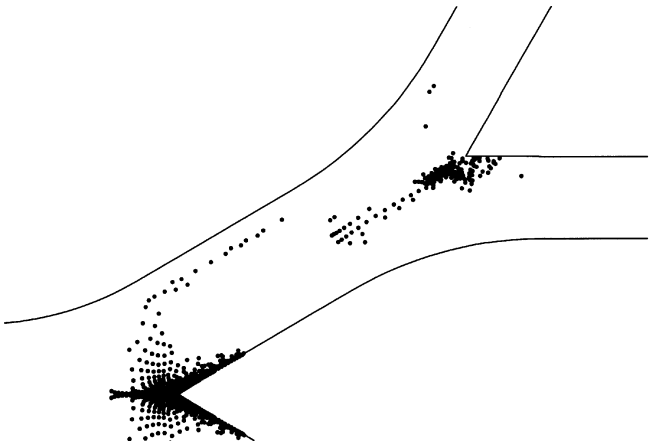

FIGURE 19. Mid-planar view of local particle deposition patterns in the planar configuration with sharp carinas at $Re_{D_1} = 2000$ and $St_{D_1} = 0.12$.

of regional particle deposition in the lung expressed as an efficiency, η =(number of particles deposited)/(total number of particles entering a region), appears to be greatly dependent on the Stokes number, measurable variations in $\eta(St)$ as well as in particle deposition patterns can be expected when changing the tubular geometry, inlet conditions in terms of air velocity profile, particle distribution, and Reynolds number, as well as particle characteristics. The present computational fluid–particle dynamics results can be summarized as follows:

(i) The particle motions in a given section of the bifurcating tubes are directly related to the corresponding secondary flows in or upstream of this section. At lower Reynolds numbers, the strength of secondary flow or vortical flow is low, so the particles can generally follow the axial air flow in a Stokes number range of $0.02 \leqslant St_{D_1} \leqslant 0.12$. With the increase in Reynolds number, the stronger secondary vortical flow may generate a particle-free zone with a higher particle concentration along the outside of this zone, due to centrifuging of particles away from vortex cores and accumulation of particles in convergence zones. With the increase in Stokes number, the particle-free zone may become larger.

(ii) The local particle deposition patterns are not significantly dependent on the inlet particle distribution but are dependent on the release positions, under the assumption of deterministic particle trajectories.

(iii) In the first bifurcation, most particles impact the carina due to the inertia force, and particles are concentrated symmetrically along the carinal ridge forming a symmetric map. However, the particle deposition patterns exhibit asymmetry in the second bifurcation due to the asymmetrically distributed flow, i.e. skewed velocity profiles. A larger number of particles deposit on the high-flow side of the second carina and a region of low particle concentration exists in the carinal ridge centre. The deposition patterns vary measurably in the second bifurcation of a 90°-non-planar configuration.

(iv) Sharp or slightly rounded carinal ridges have little effect on the deposition efficiency in the double bifurcation, but the alteration of the geometry influences the local deposition patterns to some extent.

REFERENCES

AEA Technology 1997 *CFX-4.2: Solver*. CFX International, Oxfordshire, UK.

Balásházy, I. 1994 Simulation of particle trajectories in bifurcating tubes. *J. Comput. Phys.* **110**, 11–22.

Balásházy, I. & Hofmann, W. 1993 Particle deposition in airway bifurcations – Inspiratory flow. *J. Aerosol Sci.* **24**, 745–772.

Balásházy, I. & Hofmann, W. 1995 Deposition of aerosols in asymmetric airway bifurcations. *J. Aerosol Sci.* **26**, 273–292.

Clift, R., Grace, J. R. & Weber, M. E. 1978 *Bubbles, Drops, and Particles*. Academic.

Comer, J. K. 1998 Computational two-phase flow analyses and applications to gas–liquid and gas–solid flows. PhD Thesis, Mechanical and Aerospace Engineering Department, North Carolina State University, Raleigh, NC.

Comer, J. K., Kleinstreuer, C., Hyun, S. & Kim, C. S. 2000 Aerosol transport and deposition in sequentially bifurcating airways. *Trans. ASME: J. Biomech. Engng* **122**, 152–158.

Comer, J. K., Kleinstreuer, C., Longest, P. W., Kim, C. S. & Kinsey, J. S. 1998 Computational aerosol transport and deposition analyses for human exposure chambers and model respiratory airways. ASME FED SM98, Washington, DC, pp. 1–6.

Comer, J. K., Kleinstreuer, C. & Zhang, Z. 2001 Flow structures and particle deposition patterns in double bifurcation lung models. Part 1. Air flow fields. *J. Fluid Mech.* **435**, 25–54.

Dolovich, M. 1993 Lung dose, distribution and clinical response to therapeutic aerosols. *Aerosol Sci. Tech.* **18**, 230–240.

Eaton, J. K. & Fessler, J. R. 1994 Preferential concentration of particles by turbulence. *Intl J. Multiphase Flow* **20**, Suppl. 169–209.

Farag, A., Hammersley, J., Olson, D. & Ng, T. 1998 Fluid mechanics of a symmetric bifurcation model of the human pulmonary system. ASME FED SM98, Washington, DC, pp. 1–6.

Fox, S. I. 1993 *Human Physiology*, Chap. 15. W. C. Brown Publishers, Dubuque, IA.

Gatlin, B., Cuicchi, C., Hammersley, J., Olson, D., Reddy, R. & Burnside, G. 1997 Particle path and wall deposition patterns in laminar flow through a bifurcation. ASME FED SM97, Vancouver, British Columbia, Canada, pp. 1–6.

Horsfield, K., Dart, G., Olson, D. E., Filley, G. F. & Cumming, G. 1971 Models of the human bronchial tree. *J. Appl. Physiol.* **31**, 207–217.

Johnston, J. R., Isles, K. D. & Muri, D. C. F. 1977 Inertial deposition of particles in human branching airways. In *Inhaled Particles IV*, (ed. W. H. Walton). Pergamon.

Kim, C. S. & Fisher, D. M. 1999 Deposition characteristics of aerosol particles in successively bifurcating airway models. *Aerosol Sci. Tech.* **31**, 198–220.

Kim, C. S., Fisher, D. M., Lutz, D. J. & Gerrity, T. R. 1994 Particle deposition in bifurcating airway models with varying airway geometry. *J. Aerosol Sci.* **25**, 567–581.

Kim, C. S. & Iglesias, A. J. 1989 Deposition of inhaled particles in bifurcating airway models – Inspiratory deposition. *J. Aerosol Medicine* **2**, 1–14.

Kinsara, A. A., Tompson, R. V. & Loyalka, S. K. 1993 Computational flow and aerosol concentration profiles in lung bifurcations. *Health Phys.* **64**, 13–22.

Lee, J. W., Goo, J. H. & Chung, M. K. 1996 Characteristics of inertial deposition in a double bifurcation. *J. Aerosol Sci.* **27**, 119–138.

Lonsdale, R. D. 1993 An algebraic multi-grid solver for the Navier Stokes equations on unstructured meshes. *Intl J. Numer. Meth. Heat Fluid Flow* **3**, 3–14.

Martonen, T. B., Yang, Z. & Xue, Z. Q. 1994 Effects of carinal ridge shapes on lung airstreams. *Aerosol Sci. Tech.* **21**, 119–136.

Patankar, S. V. 1983 *Numerical Heat Transfer and Fluid Flow*. Hemisphere.

Schlesinger, R. B. & Lippmann, M. 1978 Selective particle deposition and bronchogenic carcinoma. *Environ. Res.* **15**, 424–431.

Weibel, E. R. 1963 *Morphometry of the Human Lung*. Academic.

Zhao, Y., Brunskill, C. T. & Lieber, B. B. 1997 Inspiratory and expiratory steady flow analysis in a model symmetrically bifurcating airway. *Trans. ASME: J. Biomech. Engng* **119**, 52–65.

Zhao, Y. & Lieber, B. B. 1994 Steady inspiratory flow in a model symmetric bifurcation. *Trans. ASME: J. Biomech. Engng* **116**, 488–496.